Time-Resolved Contrast-Enhanced Imaging With Isotropic Resolution and Broad Coverage Using an Undersampled 3D Projection Trajectory

Andrew V. Barger,[1] Walter F. Block,[2,3]* Yuriy Toropov,[1] Thomas M. Grist,[2,4] and Charles A. Mistretta[2,4]

Time-resolved contrast-enhanced 3D MR angiography (MRA) methods have gained in popularity but are still limited by the tradeoff between spatial and temporal resolution. A method is presented that greatly reduces this tradeoff by employing undersampled 3D projection reconstruction trajectories. The variable density k-space sampling intrinsic to this sequence is combined with temporal k-space interpolation to provide time frames as short as 4 s. This time resolution reduces the need for exact contrast timing while also providing dynamic information. Spatial resolution is determined primarily by the projection readout resolution and is thus isotropic across the FOV, which is also isotropic. Although undersampling the outer regions of k-space introduces aliased energy into the image, which may compromise resolution, this is not a limiting factor in high-contrast applications such as MRA. Results from phantom and volunteer studies are presented demonstrating isotropic resolution, broad coverage with an isotropic field of view (FOV), minimal projection reconstruction artifacts, and temporal information. In one application, a single breath-hold exam covering the entire pulmonary vasculature generates high-resolution, isotropic imaging volumes depicting the bolus passage. Magn Reson Med 48:297–305, 2002. © 2002 Wiley-Liss, Inc.

Key words: fast magnetic resonance imaging; magnetic resonance angiography; undersampled projection reconstruction; contrast-enhanced MRA; time-resolved

Contrast-enhanced magnetic resonance angiography (MRA) of the chest or abdomen is typically accomplished by completing the scan in a single breath-hold to limit respiratory artifacts, and during the first pass of a contrast agent for maximum arterial enhancement (1,2). As the arterial-to-venous delay decreases, timing the bolus arrival and rapid scanning become more important. Time-resolved methods have become of increasing interest as they can mitigate the need for precise bolus timing, in addition to providing important dynamic information (3,4). Repetitive 3D Cartesian acquisitions of k-space acquired at high speed have recently generated dynamic MRA exams of the

pulmonary vasculature (5,6), and when combined with correlation postprocessing, they can be used to calculate arterial and venous image volumes (7). Time-resolved methods generally require further compromises between temporal resolution, spatial resolution, and field of view (FOV) (8). Speed is generated by acquiring less through-plane resolution or by a partial acquisition of k-space in all three dimensions.

Sparse sampling of k-space, analyzed generally in Ref. 9, has increased resolution per unit time in cases wherein the artifacts from aliased energy are acceptable due to high signal contrast. Peters et al. (10) increased in-plane resolution by a factor of 4 relative to Cartesian techniques by sampling the in-plane k-space dimensions with projections, and the slice dimension with Cartesian encoding. As is well known in computed tomography (CT), the readout resolution of the projections determines the resolution of the image, and the total number of acquired projections determines the level of artifact (11). Imaging time with these hybrid project reconstruction (PR) methods, termed PRojections Inside kZ-Encodings (PRIZE) and kZ-encoding Inside PRojections (ZIPR), was reduced to a breath-hold by limiting resolution and FOV in the slice dimension. Similar tradeoffs in coverage and slice resolution are necessary in conventional Cartesian MRA. The PRIZE method could acquire an arterial-weighted frame by acquiring the central slice encodes as the contrast first arrived. However, this method provided no temporal information and required coordinating the scan with contrast arrival.

The hybrid PR methods in Ref. 10 were later extended to provide time-resolved imaging by periodically resampling sets of projections partitioned along the slice dimension in a method termed Projection Reconstruction Time-Resolved Imaging of Contrast Kinetics (PR-TRICKS) (12). In this technique the increased speed from PR sampling was used to improve slice resolution or coverage, although large differences in volume coverage and resolution relative to the in-plane performance still existed. Tradeoffs in temporal and spatial resolution were primarily made by the resampling strategy along the k_z dimension and could not be retrospectively changed. In addition, artifacts from the signal amplitude modulation caused by varying contrast concentration are apparent primarily in the slice dimension.

Ideally, MRA in the abdomen and thorax would resemble CT angiography (CTA), whereby the entire body is easily imaged. We propose that the tradeoff in MRA between spatial resolution and coverage can be greatly reduced by acquiring data with an undersampled 3DPR tra-

[1]Department of Physics, University of Wisconsin, Madison, Wisconsin.
[2]Department of Medical Physics, University of Wisconsin, Madison, Wisconsin.
[3]Department of Biomedical Engineering, University of Wisconsin, Madison, Wisconsin.
[4]Department of Radiology, University of Wisconsin, Madison, Wisconsin.
*Correspondence to: Walter F. Block, Department of Radiology (E3/311), Clinical Sciences Center, 600 Highland Ave., Madison, WI 53792-3252. E-mail: block@mr.radiology.wisc.edu

jectory in which all three dimensions are symmetrically undersampled. 3DPR was first proposed very early in MRI (13) and has been employed successfully in imaging short T_2^* species with free induction decay (FID) readouts and MR microscopy of the lung (14–16). Fully sampled 3DPR trajectories are not widely used because the required number of excitations is prohibitively large. Although the artifact resulting from undersampling the 3DPR trajectory is structured, this aliased energy resembles noise more than coherent streaks. This is an improvement over previous hybrid 3D methods in which streaking artifacts could become significant. Undersampled 3DPR can provide for much greater volume coverage and isotropic resolution per unit time in certain applications as compared to hybrid 3D encoding. In applications where vessels lie predominantly within a thin slab, such as the peripheral arteries, the ability of the hybrid techniques to tailor the image volume is still valuable.

We also propose that oversampling the *k*-space origin has interesting possibilities for substantially reducing the tradeoffs between spatial and temporal resolution in time-resolved imaging. In 2DPR, the inherent oversampling of the central region of *k*-space has been used to retrospectively alter image contrast, and the method has been proposed for use in dynamic contrast (17,18). With the 3DPR trajectory, the *k*-space origin is sampled by every projection, and the projections can be interleaved so that all spatial frequency directions are coarsely sampled every few seconds. By temporally filtering these interleaved projections, this variable *k*-space density in 3DPR can effectively create a variable *k*-space sampling rate, a characteristic that allows for "sliding window" or TRICKS-type methods for time resolution (19,20). By reconstructing the data using a temporal aperture that widens with increasing spatial frequencies, temporal resolution with fast, flexible frame rates can be obtained without any loss in resolution or volume coverage.

In this work we present a technique termed "Vastly undersampled Isotropic Projection Reconstruction" (VIPR). We exploit the fact that for MRA, vastly undersampling the number of projections in a 3DPR trajectory can be used to limit the scan time without compromising coverage or resolution. We introduce a time-resolved method that allows for increased flexibility in timing bolus arrival and data acquisition as well as providing dynamic information. This technique should be of clinical interest because it alleviates compromises for time-resolved sequences based on imaging time, resolution, and volume coverage.

MATERIALS AND METHODS

Pulse Sequence

Data is acquired in a 3D spherical coordinate system (13), with the readout direction defined by the angle θ from the k_z-axis and by the angle φ from the k_y-axis, as shown in Fig. 1. The trajectory consists of a series of evenly spaced projections with all projections going through the origin of *k*-space. The maximum *k*-space radius value (k_{max}) determines the resolution in all three spatial directions. The radial sample spacing (Δk_r) determines the diameter of the
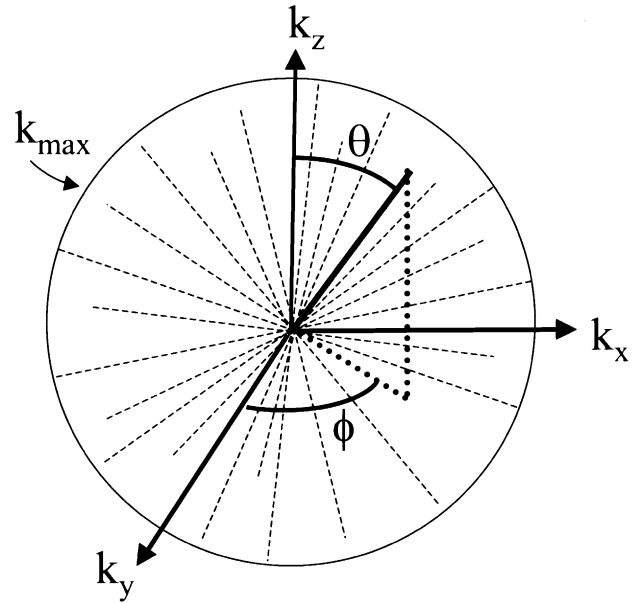

FIG. 1. Diagram of the *k*-space trajectory for a 3D projection acquisition. Each readout goes through the center of *k*-space and is defined by the angle θ relative to the k_z-axis and by the angle φ relative to the k_y-axis. Every projection samples out to the same maximum *k*-space value, k_{max}.

full FOV. The pulse sequence used to acquire data on a 3DPR trajectory was implemented on a 1.5-T MR imager (LX CardioVascular Scanner; GE Medical Systems, Milwaukee, WI) equipped with a high-performance gradient subsystem (40 mT/m maximum amplitude and 150 T/m/s maximum slew rate). If the body coil is used for excitation, a slab-selective pulse is necessary to limit signal from outside the acquired FOV. A 400-μs radiofrequency (RF) is used in this implementation. If a transmit-receive coil is used, a nonselective 200-μs RF pulse is adequate, provided that the excited region can be encompassed in the large acquired FOV in all directions. Relative to slab-selective excitation, this scheme provides a uniform flip angle across the volume, requires lower RF power, and deposits less energy into the patient. The sequence is spoiled by phase-cycling the RF excitation and by playing a dephasing gradient lobe on the *z*-axis (see Appendix).

The gradient waveforms G_x, G_y, and G_z are modulated to trace out radial lines at different θ and φ angles. The angular spacing of θ and φ is chosen such that a uniform distribution of *k*-space points is acquired (21) (see Appendix). Either full- or partial-echo readouts can be selected. If partial echo is chosen, the bottom half of *k*-space ($k_z < 0$) is only partially acquired. With a full-echo readout, either a single projection can be completely acquired, or the readout orientation can be altered or "bent" to acquire two separate half-projections for each excitation. When using a "bent" PR method, the readout initially proceeds along a single projection until the origin of *k*-space is reached. At that point, the readout gradient amplitudes are modified to acquire a nearby projection angle. The endpoints of the projections are ordered to smoothly revolve about the k_z-axis from the upper pole to the equator. By acquiring projection *n* with the left half of an echo, and projection

$n + 1$ with the right half of an echo, the change in gradient amplitude at the origin is kept to a minimum. The unacquired halves of each projection can be synthesized through homodyne processing (as described in the next section). On a high-performance gradient system, the TE and TR values for a full-echo vs. partial-echo readout are only slightly increased. Thus the bent PR method allows almost double the number of acquired projections in the same scan time relative to a partial echo acquisition. If a large number of projections are acquired, the gradient amplitude change and induced eddy-currents are minimal.

3DPR Image Reconstruction

After the scan is completed, the data is saved in a raw format and transferred to a workstation for off-line processing. The reconstruction algorithm for VIPR is based on well-known regridding techniques and places the acquired data on a 3D Cartesian grid (22). The variable sampling density of the trajectory is compensated for by weighting each data point by the square of the k-space radius at which it was acquired. All of the data is weighted in this matter without zero-filling in any dimension. The k-space origin is weighted according to the finite sphere of volume that it samples, similar to the correction proposed for 2D PR filters (23). The data is then Fourier transformed in all three directions into image space. Processing time is approximately 1 min per coil for a $256 \times 256 \times 256$ volume using a Silicon Graphics computer with four 200 MHz processors.

If a partial echo is used for the acquisition, the missing data is synthesized with a homodyne process (24,25). In the homodyne process, a low-frequency phase map is used to correct field inhomogeneity so that the symmetry of k-space data about the origin can be exploited. If a "bent" projection is acquired, a homodyne process can still be used to synthesize the missing data from each half-projection. Previous methods have been described for homodyne reconstruction of asymmetric 2DPR by synthesis of data (26,27). With the number of projections that are typically used in this application, k-space is oversampled in the central region of k-space required for the low-frequency phase map. The maximum resolution of the phase map is determined by the k-space boundary of the fully sampled central region. In our applications, we calculated phase maps with one-eighth the number of total readout points in each direction. Processing time approximately doubles with homodyne processing.

Image Artifacts From Undersampling

By Parseval's theorem, the unmeasured data results in error in the image proportional to the undersampled energy. The error energy is thus object dependent, with a "worst-case" scenario of the delta function (with equal energy at all points in k-space). In this scenario the error energy should be inversely proportional to the number of sampled projections, as can be derived from the analysis in Ref. 15. Descriptions have been provided previously (28) on how to weight the sampled data to minimize the error energy, but here we have chosen a weighting that maximizes resolution.
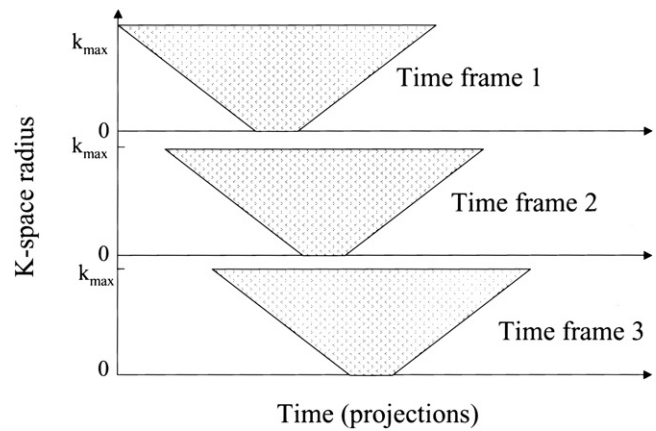

FIG. 2. The temporal k-space interpolation for generating time frames. The base of the "tornado" corresponds to the center of k-space, and the top corresponds to the outer surface of the k-space sphere in Fig. 1. The temporal size of the base and top can be chosen by the user. At higher-spatial frequencies, data from adjacent time frames are incorporated with a smoothly increasing filter. We typically used values of 4 s at the base and 26 s at the top.

Phantom studies were performed to quantify the effects of aliased energy in an arrangement designed to mimic a contrast-enhanced angiography exam. By maintaining the same scan time while imaging with different numbers of projections, we measured the error due to undersampling. A phantom consisting of two simulated carotid vessels was placed within a 12-cm FOV in a head coil. The vessels were filled with a mixture of water and gadopentetate dimeglumine (Magnevist; Schering AG, Berlin, Germany). The phantom filled the volume in the SI direction, but only 40% of the axial plane. The carotid phantom had a 70% stenosis at the origin of the internal carotid from the bifurcation. Identical volumes were prescribed and scanned with the following parameters: 30° flip angle, 28-cm FOV, ± 32 kHz bandwidth, full-echo without bent projections, and 256 readout points.

Time-Resolved Imaging

The time-resolved acquisition mode of the VIPR sequence differs from the standard sequence in the acquisition order of projections. As in a static VIPR sequence, we select a number of projections based on the total scan time and choose their endpoints to equally sample the surface of a sphere (21) (see Appendix). However, the projection acquisition order is interleaved so that spatial frequency orientations throughout the sphere are sampled on an interval less than or equal to the desired frame rate. We present a variation of a sliding-window reconstruction technique with a temporal aperture that varies with the radial distance, as shown in Fig. 2. Here the time axis is analogous to the projections acquired throughout the scan. The aperture is shaped like a tornado, with a small funnel of projections determining the low spatial-frequency information and an increasingly larger set determining higher spatial-frequency information. The oversampling of the origin of k-space in VIPR allows the base of the funnel (the temporal aperture at low spatial frequencies) to be narrow.
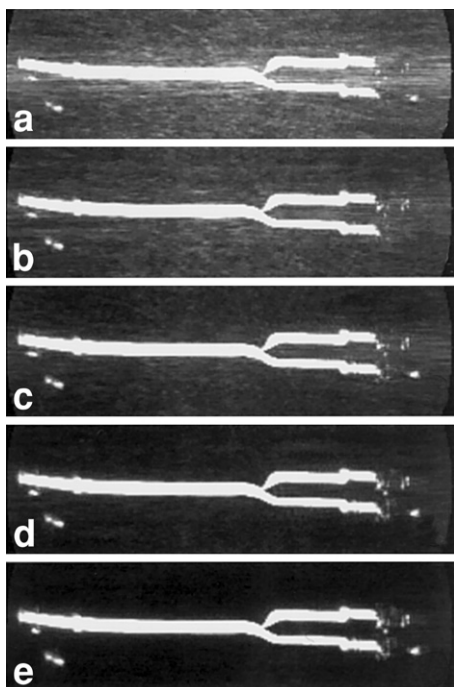
FIG. 3. Images of the stenotic carotid phantom using a VIPR sequence. Fully sampled *k*-space would require approximately 24,000 projections. The results are shown for (**a**) 1,500 projection angles with 16 signal averages, (**b**) 3,000 projection angles with 8 signal averages, and (**c**) 6,000 projection angles with 4 signal averages, (**d**) 12,000 projection angles with 2 signal averages, and (**e**) 24,000 projection angles. The stenosis is well depicted with high resolution in images **b–e**. Image **a** is somewhat degraded due to aliased energy.

The aperture widens at higher spatial frequencies to diminish the contrast-to-noise ratio (CNR) penalty from undersampling. The shape and width of the window of the "tornado" aperture can be retrospectively altered by the user to generate images with various temporal bandwidth and SNR.

Volunteer Study of Breath-Hold Imaging

For the volunteer study, institutional board approval and informed consent were obtained for 10 volunteers. An antero-posterior phased-array torso surface coil was used for signal reception and was placed to cover either the chest (five volunteers) or the abdomen (five volunteers). The amount of contrast agent used was 40 ml or 0.3 mmol of gadopentetate dimeglumine per kilogram of body weight, whichever was less. A 40-cm FOV was used, with an acquired and reconstructed isotropic resolution of 1.56 cm. A total of 10500 projections were acquired in the exam, with 1500 projections per interleave. A precontrast mask was first acquired in a single 40-s breath-hold, followed by the breath-hold acquisition with an injection of the contrast agent, injected with an automated injector (Spectris; Medrad, Pittsburgh, PA) at 1.5–2.0 ml/s. Data acquisition began approximately 4 s after injection in the pulmonary studies and 10 s after injection in the abdominal studies. No attempt was made to measure the contrast

arrival time prior to the scan or to detect the contrast arrival during the scan. The scan time for the contrast-enhanced acquisition was also 40 s. The precontrast mask was subtracted from the contrast-enhanced acquisition in *k*-space, and the resultant data were reconstructed. After the patient was placed in the scanner, the exam required approximately 10 min, including localization and coil-sensitivity scans.

RESULTS

Phantom Experiments

To separate the effects of random noise from the undersampling artifact, the carotid phantom described above was imaged with a varying number of projections. The number of signal averages in each exam was adjusted so that the total excitations equaled 24000, and the scan time was constant. The left half of the phantom is shown in Fig. 3 and is windowed to show the background signal in five exams. The number of projection angles and the number of signal averages were: 1) 1500 projection angles with 16 signal averages, 2) 3000 projection angles with eight signal averages, 3) 6000 projection angles with four signal averages, 4) 12000 projection angles with two signal averages, and 5) 24000 projection angles. The mean signal level over a region in the carotid phantom was calculated for each data set. As expected, the average measured signal for each data set was constant because the number of excitations was independent of the number of projection angles. However, the background level in the images increased with fewer projection angles due to projection artifacts, which decreased the CNR.

The alias-free FOV of the 24000 PR image (Fig. 3e) mostly contains the phantom (except for a small amount in the *z*-direction), and thus approximates fully sampled image quality. Figure 3a–d demonstrates the image quality obtained with progressive undersampling of *k*-space.
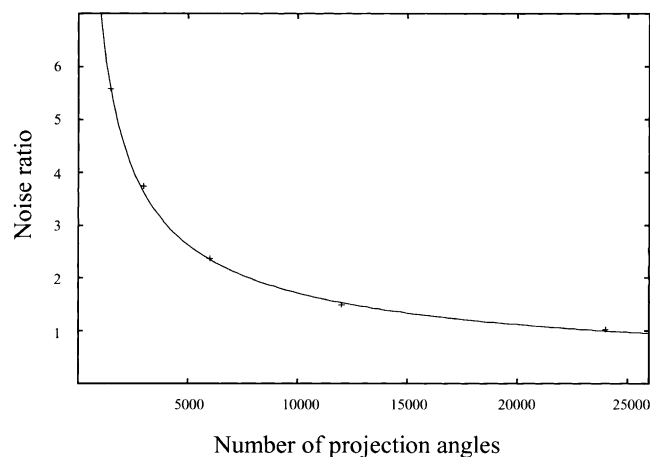

FIG. 4. Plot of the relative noise due to increased aliased energy from undersampling (points) and the best-fit curve (line). Significant degradation of image quality occurs when fewer than 15% of the number of projections required for fully sampled *k*-space. These data were obtained for the two carotid phantoms filled with contrast-enhanced water, separated by 10 cm. The noise was measured in the region between the phantoms.
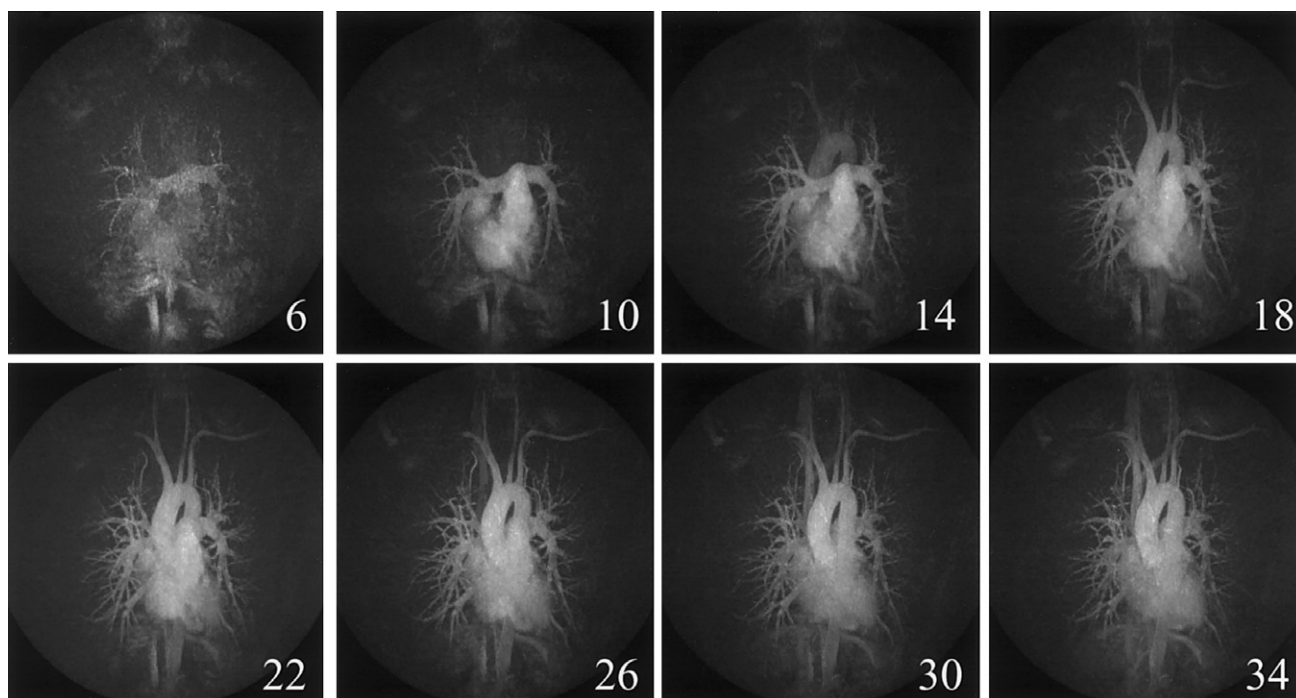
FIG. 5. Temporal processing of the VIPR projections generates a set of time-resolved image volumes. Coronal MIPs of these volumes are annotated with the time after contrast injection. The frames depict passage of the contrast from the pulmonary arteries, through the pulmonary veins and into the aorta and great vessels.

Two 24000 projection scans were subtracted in *k*-space and then reconstructed to obtain an estimate of the noise not related to PR artifact. The mean background noise of each individual scan relative to that of the subtracted data set was then calculated in a region between the carotid phantoms. The mean noise is plotted in Fig. 4 as a function of number of projection angles (cross marks), N_p. Also shown is the best-fit curve a/N_P^b (solid line), with the value $b = 0.62$. The decrease in CNR due to undersampling is less than would be expected for a delta function object.

Volunteer Studies

The characteristics of the VIPR sequence are illustrated in pulmonary and abdominal MRA exams of volunteers. The sequence used a full-echo acquisition with "bent" projections resulting in TR and TE values of 3.8 ms and 1.5 ms, respectively. The sampling bandwidth was ± 125 kHz, and a flip angle of 30° was used. The VIPR scan used 10500 excitations (21000 projections) and acquired a 40 × 40 × 40 cm volume with a 256 readout matrix, reconstructed to a final 256 × 256 × 256 volume.

Figure 5 shows time-resolved maximum intensity projection (MIP) images from a VIPR pulmonary exam annotated with the time after contrast injection. Time resolution of the passage of contrast is shown in these images, with the progression of contrast-enhancement of the pulmonary arteries (10 s), pulmonary veins (14 s), arch of aorta (18 s), and great vessels (22 s). The broad coverage of

FIG. 6. The arterial image volume shown at 10 seconds after injection in Fig. 5 is rotated to show isotropic resolution MIPs in three different orientations. The images demonstrate good venous suppression and a comprehensive FOV.
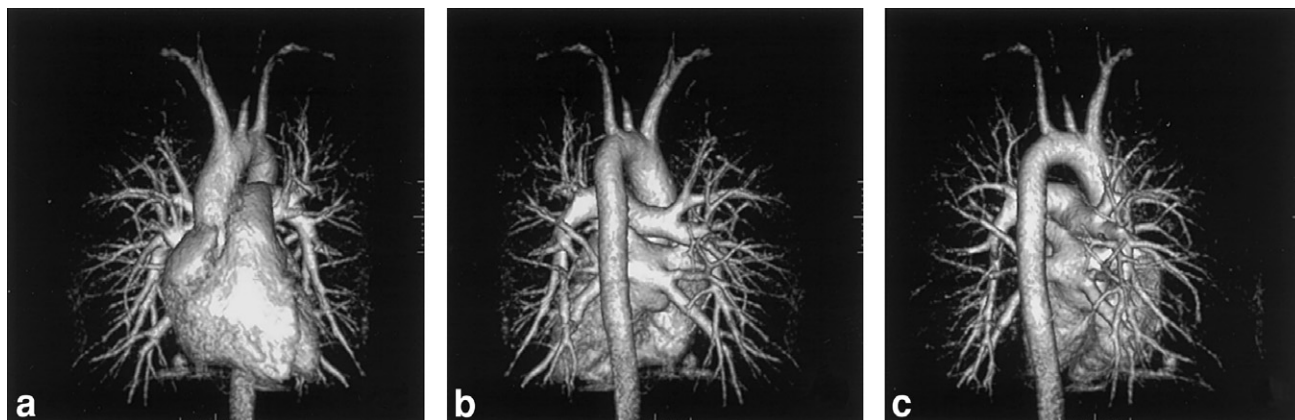
FIG. 7. The isotropic resolution provided by VIPR facilitates volume rendering. Here all the projections from a breath-hold are combined with equal weighting to display a combination of arterial and venous vessels in the (**a**) AP view, (**b**) PA view, and (**c**) oblique view.

the VIPR scan allows the entire pulmonary vasculature to be included in the imaged FOV. Even though the time between enhancement of the arteries and veins is quite short, venous suppression can be obtained. Arbitrary reformatted images can then be generated for any given time-frame, as shown in Fig. 6 for the pulmonary arteries (10 s). In Fig. 7, the temporal data is equally weighted and volume-rendered to demonstrate a high-resolution anterior view of the pulmonary arteries, veins, and aorta. Figure 7b shows a view from a posterior orientation, while Fig. 7c shows a view from an oblique orientation. The spatial resolution is constant from all orientations.

The effect of the shape of the temporal filter on CNR is shown in Fig. 8 for an arterial time frame. The data set shown in Fig. 6 was reconstructed with a varying width of the top of the temporal filter. The width of the base remained constant at 4 s. The CNR for a slice containing the pulmonary artery is plotted vs. the top width of the temporal filter. As expected, CNR increases as the inclusion of higher spatial frequencies from a greater number of projections reduces the aliased, undersampled energy.

Figure 9 shows images from an abdominal scan of a volunteer with the VIPR sequence, which was completed in a single 40-s breath-hold. Again the scan used 10500 excitations (21000 projections) and acquired a 40 × 40 × 40 cm volume with a 256 readout matrix. Relative to the lungs, additional static structures create more unsampled, aliased energy that decreases CNR. This problem is mitigated by viewing the exam from a workstation with MIPs of limited thickness. In the limited MIP shown in Fig. 9a, all of the acquired projections were used in the reconstruction. There is subsequently a large amount of venous contamination of the resultant image. In the limited MIP shown in Fig. 9b, a 4-s time frame was used for the reconstruction (4-s low spatial-frequency width, 40-s high spatial-frequency width) and the increase in contrast between the arterial signal and venous signal is readily apparent. Of course, any time frame may be selected. For example, by selecting a time frame from approximately 20 s after peak arterial enhancement, a venous image could also be obtained. Figure 9c shows a sagittal view of the same reconstruction seen in Fig. 9b. This demonstrates that the coverage of the scan also includes the entire body in the anterior-posterior direction. The in-plane reconstructed resolution of the sagittal image is equal to that of the coronal image

DISCUSSION

This research demonstrates that by using the VIPR method it is possible to obtain high-resolution, time-resolved, contrast-enhanced MRA scans with broad coverage. Repeatedly sampling the low spatial frequencies allows for a unique form of temporal image filtering. The shape and width of the temporal filter can be chosen retrospectively, in contrast to the fixed time-frames provided by the PR-TRICKS method. By integrating more high spatial-frequency information from adjacent excitations, the level of artifact in each time frame can be retrospectively reduced to allow for diagnostic image quality. While PR-TRICKS resampled the central slice encoded every 9 s and then used view-sharing to double the frame rate, VIPR has successfully created time-frames whose lowest spatial frequencies are completely resampled every 4 s. The width of the temporal filter at the *k*-space origin is theoretically limited to a single TR.
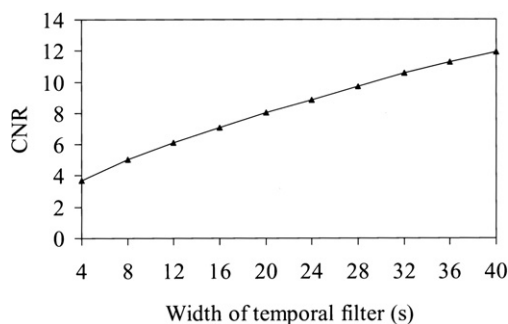

FIG. 8. The effect of increasing the width of the top of the temporal filter is shown. A data set of the pulmonary vasculature was reconstructed with the maximum width of the temporal filter varying from 4 to 40 seconds. Using an image located at isocenter which contained a large segment of the pulmonary artery, two regions containing artery and background were used to calculate the CNR for each reconstruction.
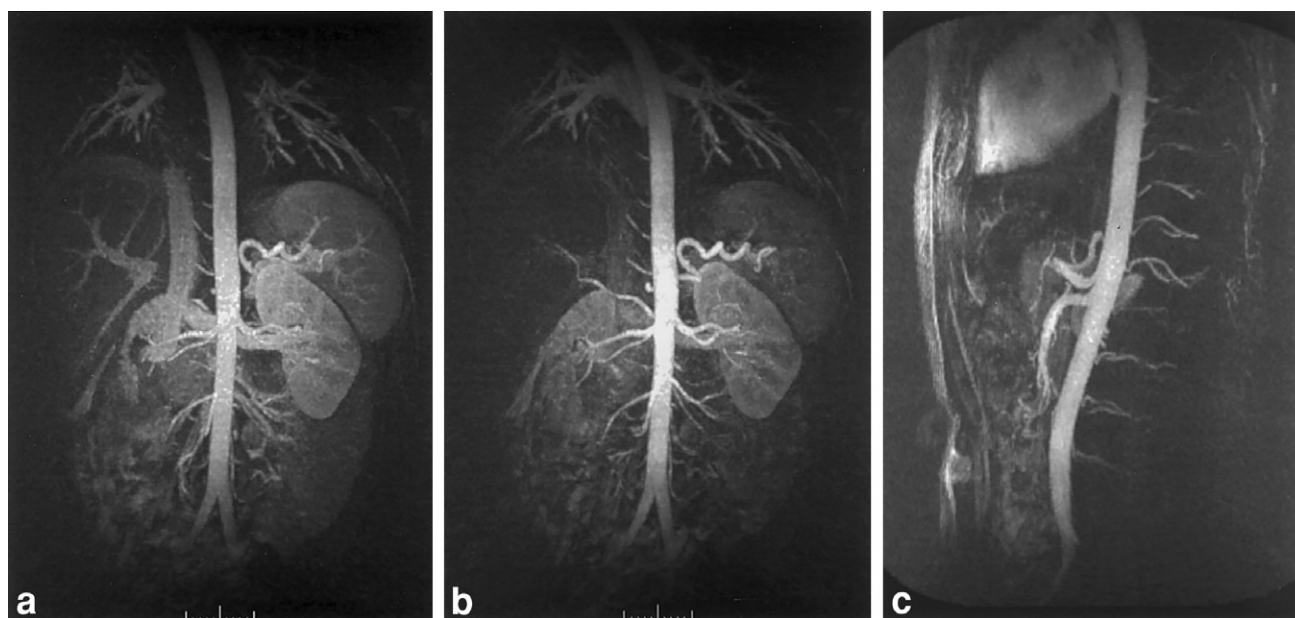
FIG. 9. Demonstration of VIPR images of the abdominal vasculature using 0.3 mmol/kg of contrast agent, completed in a single breath-hold. The image in **a** is a limited MIP using all the time-frames, and substantial venous contamination is seen. In **b** the time frame with maximal arterial contrast is shown. Venous signal is greatly reduced as compared with **a** without a loss in resolution. The sagittal view seen in **c** demonstrates the large FOV of the VIPR acquisition, with isotropic resolution in any reconstructed plane.

When imaging the chest we were able to view the progression of contrast through the cardiac and pulmonary systems, while each time frame still maintained very high resolution. With an abdominal imaging application, we were able to retrospectively choose the best time frame for maximal arterial contrast. No dose-timing scan or automated bolus detection was required before beginning imaging. The only remaining requirement in this case is coordinating the breath-hold approximately with the bolus arrival. The temporal processing methods allow for venous suppression, but further study is needed to compare its effectiveness to single time-frame methods such as elliptical centric encoding (29). Another benefit of repeatedly sampling the spatial frequencies near the k-space origin is less sensitivity to motion and arterial pulsatility (30).

There is no penalty in terms of coverage or spatial resolution. As was previously discussed, the resolution of a 3DPR image is determined by the readout resolution. Although VIPR sparsely samples PRs to minimize scan time, there is still isotropic resolution across the volume. The resolution limits using VIPR are not constrained by scan time, but rather by noise and artifact, as decreased voxel size and increased aliased energy will decrease both SNR and CNR. Images acquired with Fourier encoding typically have the highest resolution along the readout direction and lower resolution along the other directions. In the hybrid PR methods (10), the slice thickness ranged from four to eight times higher than the relatively small in-plane voxel dimensions. Although non-isotropic imaging can have high resolution in the imaged plane, the resolution of reformatted views is limited by the lowest-resolution dimension. This is significant because it has been shown that the sensitivity and specificity of abdominal contrast-enhanced 3D angiography is greatly improved by viewing multiplanar reformats in addition to viewing the MIP in the acquired plane (31). Since most arteries do not lie completely in the acquired plane, we speculate that the isotropic resolution of VIPR should prove to be very advantageous for reformatted images. For example, a renal artery stenosis could be observed with equally high resolution around a 360° view. The sequence is equally sensitive to spatial frequencies in any orientation, which is not possible when partial Fourier acquisitions are used in more than one k-space dimension. Since each spatial dimension is coded similarly to the others, there is no preferred direction for motion ghosts or artifacts from varying contrast concentration during the scan.

Another benefit of the VIPR method is that the coverage of the exam is greatly improved over Fourier imaging. For example, a conventional 3D-FT exam requires careful positioning of a relatively narrow scan plane to ensure that objects of interest are included in the volume. Other anatomical structures that lie outside this limited region cannot be acquired with the same contrast injection. Likewise, the hybrid PR methods, PRIZE and ZIPR (10), prescribed slabs whose thickness was a quarter to a third of the in-plane FOV. The volume coverage of 3DPR retains the full FOV uniformly in all three directions. For the contrast-enhanced abdominal exam, the 40-cm full FOV covered the whole abdomen without any need for placing a targeted volume of acquisition. The mesenteric and the lumbar arteries were included in the extremely large FOV. As another example, the scan of the chest using the VIPR sequence was able to acquire the entire pulmonary vasculature with a single injection of contrast.

The breath-hold duration of our volunteer scans is currently too long for many clinical exams. However, reducing the 40-s breath-holds to 15–20 s is a reasonable goal.

TR reduction methods have resulted in TRs as low as 1.6 ms (5,6), and we expect that optimizing the sequence programming could reduce the VIPR TR from 3.8 ms to 2.6 ms for a full-echo acquisition. Randomizing the locations of the sampled PRs may also decrease scan time by further decorrelating the undersampled energy (32). Our spherical FOV also does not take into account the cylindrical shape of the human torso. Methods exist to create an ellipsoidal FOV that could reduce the number of necessary excitations by one-third (33). It has been shown that variable density k-space sampling can be applied to arbitrary 2D trajectories, such as spiral readouts (9). Other trajectories can be applied in the 3D case as well, such as a "cone" trajectory wherein the surfaces of concentric cones are traversed with a spiral-like trajectory (34). The benefits of these alternate trajectories, such as fewer excitations being required, could then be realized. To obtain temporal information as described in this work, however, does require that the trajectory repeatedly sample spatial frequencies near the k-space origin.

The major limitation of the VIPR technique is that artifacts from undersampling decrease CNR. The limited CNR is demonstrated in the vessel dropout in the right, upper, second bifurcation in Fig. 6, and in the lumbar vessels in Fig. 9. In the VIPR technique, a reduced well-constructed FOV is centered around each object with superimposed aliased energy from other objects. With VIPR coherent structured artifacts are in general not observed, although long edges present in phantoms can give rise to streaks. Through phantom experiments and clinical exams, we have found that as long as approximately 10–20% of the projections defined by the Nyquist criteria are acquired, the CNR penalty for breath-hold contrast-enhanced applications is not limiting. Using the "bent" projection method improves the image quality by effectively sampling more projections. Although this method does increase the TE, current high-performance gradients allow the TE to be maintained at values acceptable for limiting flow-dephasing in contrast-enhanced applications. In addition, the methods described earlier for shortening the scan time will also reduce the amount of undersampled energy and decrease the need to create MIPs of limited thickness. Artifact reduction algorithms could be used to further improve image quality (35).

The unique properties of VIPR require further studies on the implications for the clinical acquisition and evaluation of MRA data. The time resolution of the sequence means that a dose-timing scan is not required in many situations. The placement of the imaging volume for the 3DPR acquisition requires simply centering the acquisition within the coil-sensitivity region. Because no detailed scan volume placement is required, even the localizer could be eliminated. In addition, the radiologist can retrospectively choose any oblique plane within the large FOV and obtain the same resolution. In the future, the VIPR method could be a significant factor in reducing the cost and increasing the efficiency of MRA examinations. A larger-scale clinical study is currently underway to completely evaluate the potential of the technique in terms of both data acquisition and evaluation.

APPENDIX

The sequence is spoiled by phase-cycling the RF pulse and playing a dephasing lobe on one gradient axis. The area of the dephasing lobe is calculated to satisfy the condition

$$\int_0^{TR} (G_{dephase}(t) + G_{read}(t))dt = n \cdot k_{max} \qquad [1]$$

where $n \geq 2$ (36). Because the read gradient is always positive on the logical z-axis, the time required for the spoiling gradient is minimized by playing the dephasing lobe only on G_z. The G_x and G_y gradients are rewound to maintain a steady state.

The projection angles must be selected to uniformly cover k-space. An algorithm evenly distributes the projections by sampling the spherical surface with a spiral trajectory, with the conditions of constant path velocity and surface area coverage (21). This solution also has the benefit of generating a continuous sample path, which reduces gradient switching and eddy currents. For N total projections, the equations for the gradient amplitude as a function of projection number n are

$$G_z(n) = \frac{2n - 1}{2N} \qquad [2a]$$

$$G_x(n) = \cos(\sqrt{2N\pi} \, \sin^{-1} G_z(n)) \sqrt{1 - G_z(n)^2} \qquad [2b]$$

$$G_y(n) = \sin(\sqrt{2N\pi} \, \sin^{-1} G_z(n)) \sqrt{1 - G_z(n)^2} \qquad [2c]$$

where the equations reflect the fact that the projections are acquired as full or fractional echoes instead of FIDs.

REFERENCES

1. Earls JP, Rofsky NM, DeCorato DR, Krinksy GA, Weinreb JC. Breath-hold single-dose gadolinium-enhanced three-dimensional MR aortography: usefulness of a timing examination and MR power injector. Radiology 1996;201:705–710.
2. Hany TF, McKinnon GC, Leung DA, Pfammatter T, Debatin JF. Optimization of contrast timing for breath-hold three-dimensional MR angiography. J Magn Reson Imaging 1997;7:551–556.
3. Carroll TJ, Korosec FR, Petermann GM, Grist TM, Turski PA. Carotid bifurcation: evaluation of time-resolved three-dimensional angiography. Radiology 2001;220:525–532.
4. Hany TF, Carroll TJ, Omary RA, Esparza-Coss E, Krosec FR, Mistretta CA, Grist TM. Contrast-enhanced, single-injection MRA with automated table movement compared to multi-injection, time-resolved CE 3D-MRA of the aorta and run-off vessels—initial results. Radiology 2001;220:266–273.
5. Goyen M, Laub G, Ladd M, Debatin J, Barkhausen J, Truemmler K, Bosk S, Ruehm S. Dynamic 3D MR angiography of the pulmonary arteries in under four seconds. J Magn Reson Imaging 2001;13:372–377.
6. Carr J, McCarthy RM, Laub G, Pereles S, Finn JP. Subsecond contrast-enhanced 3D MR angiography: a new technique for dynamic imaging of the vasculature. In: Proceedings of the 9th Meeting of ISMRM, Glasgow, Scotland, 2001. p 302.

7. Schoenberg S, Bock M, Floesser F, Grau A, Williams D, Laub G, Bosk S, Knopp MV. High resolution pulmonary arteries and venography using multiple bolus, multiphase 3D-Gd-MRA. J Magn Reson Imaging 1999; 10:339−346.

8. Mistretta CA, Grist TM, Korosec FR, Frayne R, Peters DC, Mazaheri Y, Carroll TJ. 3D time-resolved contrast-enhanced MR DSA: advantages and tradeoffs. Magn Reson Med 1998;40:571−581.

9. Tsai CM, Nishimura DG. Reduced aliasing artifacts using variable-density *k*-space sampling trajectories. Magn Reson Med 2000;43:452−458.

10. Peters DC, Korosec FR, Grist TM, Block WF, Vigen KK, Holden JE, Mistretta CA. Undersampled projection reconstruction applied to MR angiography. Magn Reson Med 2000;43:91−101.

11. Joseph P, Whitley J. Experimental simulation of ECG-gated heart scans with a small number of views. Med Phys 1983;10:444−449.

12. Vigen KK, Peters DC, Grist TM, Block WF, Mistretta CA. Undersampled projection-reconstruction imaging for time-resolved contrast-enhanced imaging. Magn Reson Med 2000;43:170−176.

13. Lai CM, Lauterbur PC. True three-dimensional image reconstruction by nuclear magnetic resonance zeugmatography. Phys Med Biol 1981;26: 851−856.

14. Glover G, Pauly J, Bradshaw K. Imaging 11B with a 3D projection reconstruction method. J Magn Reson Imaging 1992;2:47−52.

15. Shattuck MD, Gewalt SL, Glover GH, Hedlund LW, Johnson GA. MR microimaging of the lung using volume projection encoding. Magn Reson Med 1997;38:938−942.

16. Viallon M, Cofer GP, Suddarth SA, Moller HE, Chen XJ, Chawla MS, Hedlund LW, Cremillieux Y, Johnson GA. Functional MR microscopy of the lung using hyperpolarized 3He. Magn Reson Med 1999;41:787−792.

17. Song HK, Dougherty L. *k*-Space weight imaged contrast (KWIC) for contrast manipulation in projection reconstruction MRI. Magn Reson Med 2000;44:825-832.

18. Altbach MI, Theilmann RJ, Kono M, Troward TP, Outwater EK, Gmitro AF. A T$_2$-weighted radial MRI method for imaging the abdomen. In: Proceedings of the 9th Annual Meeting of ISMRM, Glasgow, Scotland, 2001. p 2016.

19. Korosec FR, Frayne R, Grist TM, Mistretta CA. Time-resolved contrast-enhanced 3D MR angiography. Magn Reson Med 1996;36;345−351.

20. Riederer SJ, Tasciyan T, Farzaneh F, Lee JN, Wright RC, Herfkens RJ. MR fluoroscopy: technical feasibility. Magn Reson Med 1988;8:1−15.

21. Wong S, Roos M. Strategy for sampling on a sphere with applications to 3D selective pulse design. In: Proceedings of the 12th Annual Meeting of SMRM, New York, 1993. p 1178.

22. Jackson JI, Meyer CH, Nishimura DG, Macovski A. Selection of a convolution function for Fourier inversion using gridding. IEEE Trans Med Imaging 1992;10:473−478.

23. Lauzon ML, Rutt BK. Effects of polar sampling in *k*-space. Magn Reson Med 1996;36:940−949.

24. Noll D, Nishimura D, Macovski A. Homodyne detection in magnetic resonance imaging. IEEE Trans Med Imaging 1991;10:154−163.

25. Block WF, Peters DC, Vigen KK. Homodyne reconstruction for projection reconstruction trajectories. In: Proceedings of the 7th Annual Meeting of ISMRM, Philadelphia, 1999. p 659.

26. Noll D, Pauly J, Nishimura D, Macovski A. Magnetic resonance reconstruction from projections using half the data. SPIE 1991;1443:29−36.

27. Boada FE, Christensen JD, Gillen JS, Thulborn KR. Three-dimensional projection imaging with half the number of projections. Magn Reson Med 1997;37:470−477.

28. Pipe JG. Reconstructing MR images from undersampled data: data-weighting considerations. Magn Reson Med 2000;43:867−875.

29. Riederer SJ, Fain SD, Kruger DG, Busse RF. Three dimensional contrast-enhanced magnetic resonance angiography using fluoroscopic triggering and elliptical centric view ordering. Int J Card Imaging 1999; 15:117−129.

30. Glover GH, Pauly JM. Projection recontruction techniques for reduction of motion effects in MRI. Magn Reson Med 1992;28:275−289.

31. Hany TF, Schmidt M, Davis CP, Gohde SC, Debatin FJ. Diagnostic impact of four postprocessing techniques in evaluating contrast-enhanced three-dimensional MR angiography. AJR Am J Roentgenol 1998;170:907−912.

32. Wilbur BS, Jeong EK, Parker DL. Random angular undersampling projection reconstruction for high resolution 3D CE-MRA. In: Proceedings of the 12th Annual Meeting of MR Angiography Club, Madison, 2001. p 18.

33. Kust MP, Shattuck MD, Glover GH, Johnson GA. Anisotropic methods for three-dimensional projection magnetic resonance imaging. In: Proceedings of the 5th Annual Meeting of ISMRM, Vancouver, Canada, 1997. p 1996.

34. Irarrazabal P, Nishimura DG. Fast three dimensional magnetic resonance imaging. Magn Reson Med 1995;33:656−662.

35. Holden JE, Unal O, Peters DC, Oakes TR. Control of angular undersampling artifacts in projection-based MR angiography by iterative reconstruction. In: Proceedings of the 8th Annual Meeting of ISMRM, Denver, 2000. p 1827.

36. Haacke E, Brown R, Thompson M, Venkatesan M. Magnetic resonance imaging. New York: John Wiley and Sons, Inc.; 1999. p 510.